



# Analysis of microstructure and mechanical performance of polymeric cellular structures designed using stereolithography

Sofiane Guessasma<sup>a,b,\*</sup>, Liu Tao<sup>b</sup>, Sofiane Belhabib<sup>c</sup>, Jihong Zhu<sup>b</sup>, Weihong Zhang<sup>b</sup>, Hedi Nouri<sup>d</sup>

<sup>a</sup> INRA, UR1268 Biopolymères Interactions Assemblages, F-44300 Nantes, France

<sup>b</sup> Laboratory of Engineering Simulation & Aerospace Computing-ESAC, Northwestern Polytechnical University, 710072 XiAn, Shaanxi, China

<sup>c</sup> LUNAM University of Nantes Angers Le Mans, CNRS, GEPEA, UMR 6144, IUT de Nantes, 2 avenue du Professeur Jean Rouxel, 44475 Carquefou Cédex, France

<sup>d</sup> Department of Polymers and Composites Technology & Mechanical Engineering, Mines Douai, 941 rue Charles Bourseul, CS 10838, F-59508 Douai, France

## ARTICLE INFO

### Keywords:

Stereolithography  
Finite element computation  
Compressive response  
Cellular polymer  
X-ray micro-tomography  
Damage – densification model

## ABSTRACT

The aim of this work is to deliver a precise statement about the mechanical effect of microstructural defects induced by stereolithography. Design of cellular structures based on a photosensitive resin with varied porosity content is performed up to 60%. The compressive behaviour of these structures is captured and microstructural defects are analysed using X-ray micro-tomography. Finite element computation is considered to predict the compressive behaviour of both 3D microstructures and CAD (Computer-Aided Design) models up to the densification stage. X-ray micro-tomography analyses reveals that two main defects are generated by the process, namely residual support material and excess of resin trapped inside the porous network. Significance of the defects is proved to be related to the design of cellular structures with porosity levels in the range 10–30%. In addition, both experimental and numerical results show no evidence of anisotropic effect related to additive layering of resin. Finally, the suggested damage – densification constitutive law captures the main characteristics of the compressive response of studied cellular structures.

## 1. Introduction

Cellular solids, which are media composed of solid and gaseous phases, have particular performance that can be modulated in a wide range by manipulating their airy nature [1]. Indeed, cellular solids are widely used in applications requiring lightweight performance [2], thermal insulation [3], energy and noise absorption [4], filtering (Yadroitsev et al., 2009), and substitutes for tissue engineering [5]. These applications impose stringent restrictions on the cellular morphology. Conventional manufacturing methods like foaming and powder metallurgy experience difficulties to control the internal microstructural cellular structures, causing the low repeatability of desired morphology and deviation from targeted properties. Therefore, the obtained properties are highly sensitive to scale change because of the differences that appear between local and global measurements such as for density, feature size and shape. Additive manufacturing (AM) allows the fabrication of parts exhibiting complex geometries. On top of being reproducible, these AM parts share the key advantage of offering predictable and pre-determined unit cells even with interconnected porous structures [6].

Some of the most popular AM systems include stereolithography (SL), laser sintering (LS), fused deposition modelling (FDM) and

laminated object manufacturing (LOM), which use liquid, filament/paste, powder and solid sheet material, respectively [7]. Stereolithography (SL) is one of these AM techniques, which exhibit high fabrication accuracy. The increasing number of available materials that are now used as a feedstock material for stereolithography allows stereolithography to fairly compete with traditional process routes for polymer manufacturing. Stereolithography has received remarkable success in applications of manufacturing porous structures for tissue engineering [8]. Processes of SL are integrated manufacturing processes, which include model slicing, laser devices control, materials, machine parameter setup, and post-processing modules [9]. SL process like the other AM technologies presents some imperfections in dealing with filling the space of the part without the generation of discontinuities. Such imperfections ranges from geometrical defects to volume mismatch. These defects impair the effectiveness of the AM process and in turn affect the performance of the designed parts. If the previously mentioned imperfections are genuine kinematics defects, another type is more specific to SL, namely inhomogeneous curing. This is the source for distortion and shrinkage phenomena that appear during the post-curing process. Dimension inaccuracy originates here from the uncured or partially cured resin within the photopolymer material [10]. Because of all mentioned imperfections, engineering

\* Corresponding author. INRA, UR1268 Biopolymères Interactions Assemblages, F-44300 Nantes, France.

E-mail addresses: [sofiane.guessasma@inra.fr](mailto:sofiane.guessasma@inra.fr) (S. Guessasma), [JH.Zhu\\_FEA@nwpu.edu.cn](mailto:JH.Zhu_FEA@nwpu.edu.cn) (J. Zhu), [zhangwh@nwpu.edu.cn](mailto:zhangwh@nwpu.edu.cn) (W. Zhang).

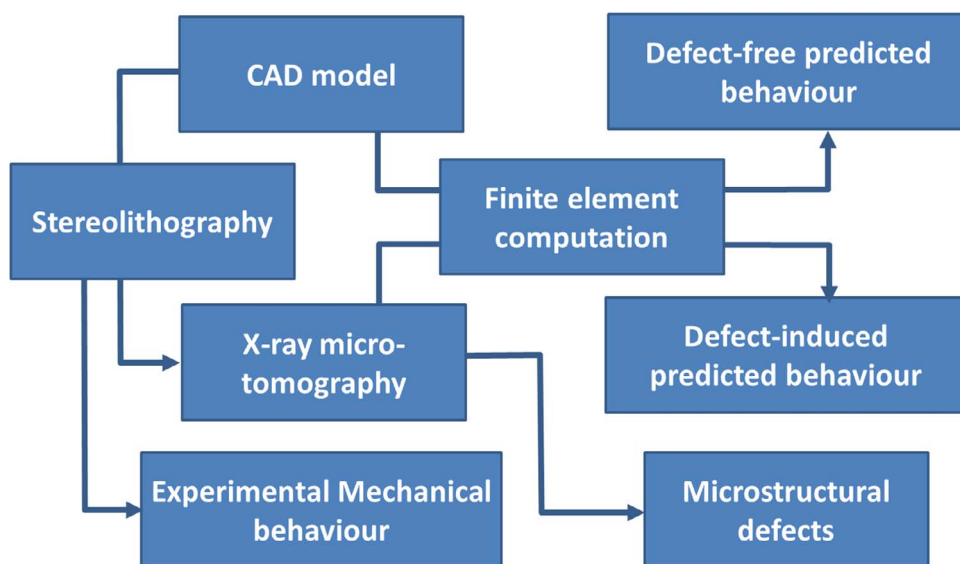


Fig. 1. General scheme of the approach used to derive the effect of process induced defects on mechanical performance of cellular parts with close porosities designed using stereolithography.

parameters received major attention for the purpose to optimise the process and improve the quality of the manufactured parts. In most situations arising, compromises are found. Slicing the CAD model prior printing is a typical example. Indeed, a small slice thickness leads to accurate geometry but large build time, while large slice thickness causes dimension errors and unsatisfying surface finish state due to staircasing. Several strategies have been developed to optimize the slicing procedure including direct slicing of CAD models with constant or adaptive layering thickness [11]. Physical parameters such as hatch cure depth, blade gap, hatch spacing and orientation have also been studied due to their large effect on the part quality. Zhou et al. [12] report five possible input process parameters that affect geometry accuracy with a leading influence of layer thickness and laser scanning duration. Chockalingam et al. [13] confirm the influential effect of layer thickness on mechanical properties of SL components more particularly residual stress and tensile strength. Build orientation as another process parameter directly affects the part accuracy, mechanical performance, build time and cost. Quintana et al. [14] demonstrate through a statistical design of experiments that the layout has a significant influence on tensile strength and stiffness. In fact, the layout influence is justified by the relative positioning of the layers composing the part with respect to the loading direction.

These flaws mentioned above are amplified when it comes to the design of cellular structures. The associated complex surface tessellation undermines the fabrication step more severely compared to dense structures. This problem is critical because of the large sensitivity of the in-service performance to cellular characteristics [15]. The amount of voids, for instance, tunes exponentially both strength and stiffness [16,17]. It appears then important to precisely quantify the influence of the complex porous architecture on the mechanical performance of SL-based parts. Analytical methods are often limited to predict such rendering of complex architectures, while numerical approaches like finite element (FE) method are more accurate especially to incorporate microstructural details [18]. This strategy of using FE based models is applied by Campoli et al. [19] to evaluate the mechanical performance of cellular structures manufactured using selective melting. To be even more effective, FE computations are to be coupled with adequate 3D imaging techniques to access microstructural defects. Veyhl et al. [20] point out the mechanical anisotropy of cellular structures that can be reached using FE models combined with micro-computed tomography.

As shown in Fig. 1, the sensing of the microstructural defect role on part performance is considered through a scheme involving 3D imaging, finite element computation and mechanical testing. The idea here is to compare the predicted behaviour of the cellular structures based

on implementation, in the finite element model, of microstructural information issued from 3D imaging.

This defect based model is compared to predictions relying on CAD model geometries. The difference between the two predictions is informative of microstructural defect influence, which is precisely evaluated and quantified in this study. The comparison with the experimental testing result (Fig. 1) provides a key understanding of the role of defects in driving the performance of porous parts designed using stereolithography.

## 2. Experimental layout

### 2.1. Cellular structure processing

The cellular solids are designed using sequential addition algorithm based on random positioning of voids with typical diameter of nearly 10 mm each. The spherical porosities are allowed to overlap to increase the porous content from 0 up to 60%. In order to guarantee structural stability of the cellular material, void positioning is accepted at the condition of solid material continuity. The CAD models of typical dimensions of  $(30 \times 30 \times 30) \text{ mm}^3$  are converted into stl files. The

Table 1  
Photosensitive resin SPR6000B: Physical characteristics of the liquid and post-cured states.

<i>Liquid state</i>		
Appearance		White
Density		1.13 g/cm <sup>3</sup> at 25 °C
Viscosity		355 cps at 28 °C
Penetration distance, Dp		0.145 mm
Critical exposure energy, Ec		9.3 mJ/cm <sup>2</sup>
Building layer thickness		0.1 mm
<i>Post-cured solid state (90-min UV post-cure)</i>		
Property	Test standard	Magnitude
Hardness, Shore D	ASTM D 2240	83
Flexural modulus	ASTM D 790	2692–2775 MPa
Flexural strength	ASTM D 790	69–74 MPa
Tensile modulus	ASTM D 638	2189–2395 MPa
Tensile strength	ASTM D 638	27–31 MPa
Elongation at break	ASTM D 638	12–20%
Impact strength	ASTM D 256 (notched Izod)	58–70 J/m
Heat deflection temperature	ASTM D 648 at 66 psi	52 °C
Glass transition (Tg)	DMA, E''peak	62 °C
Coefficient of thermal expansion	TMA (T < Tg)	97 × 10 <sup>-6</sup> /°C
Density	–	1.16 g/cm <sup>3</sup>

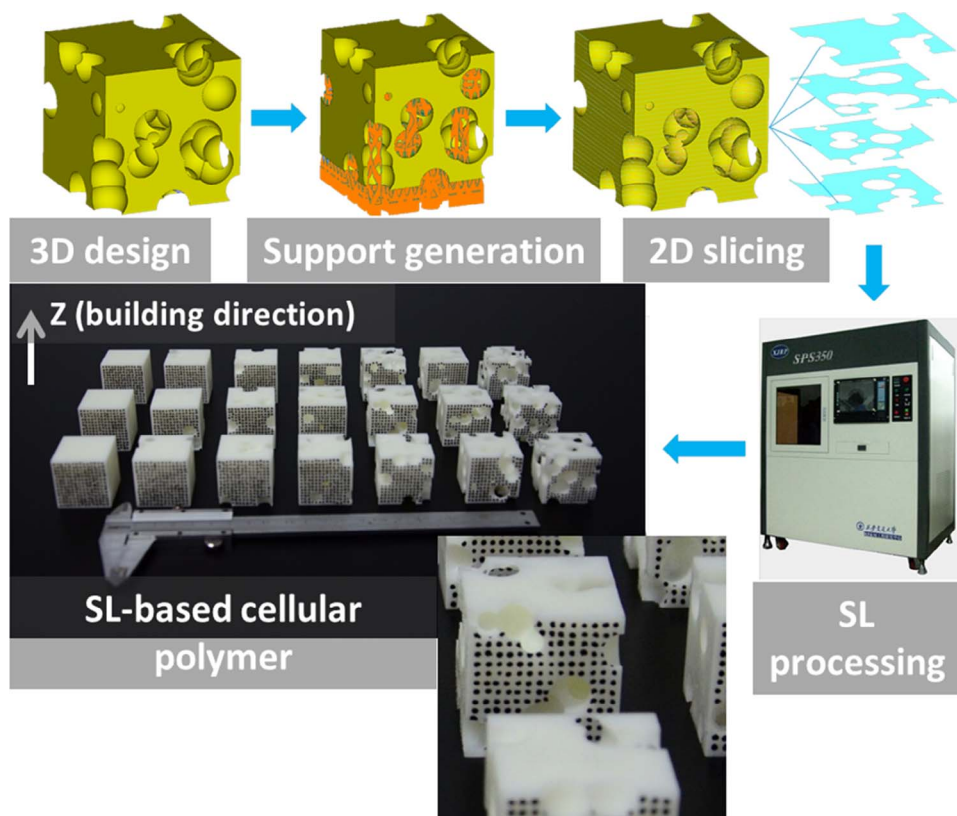


Fig. 2. Main steps to achieve SL-based cellular materials.

virtual models are sliced into 0.1 mm in thickness layers to define the different horizontal cross sections. The sliced models are processed using SL equipment purchased from Hengtong Ltd, China under the reference SPS350B. Laser beam of diameter 0.15 mm and wavelength of

355 nm is used to cure the photosensitive resin. The main characteristics of the liquid resin (SPR6000 epoxy from Hengtong Ltd, China) and cured polymer are given in Table 1.

The laser draws the pattern according to the slicing data with a

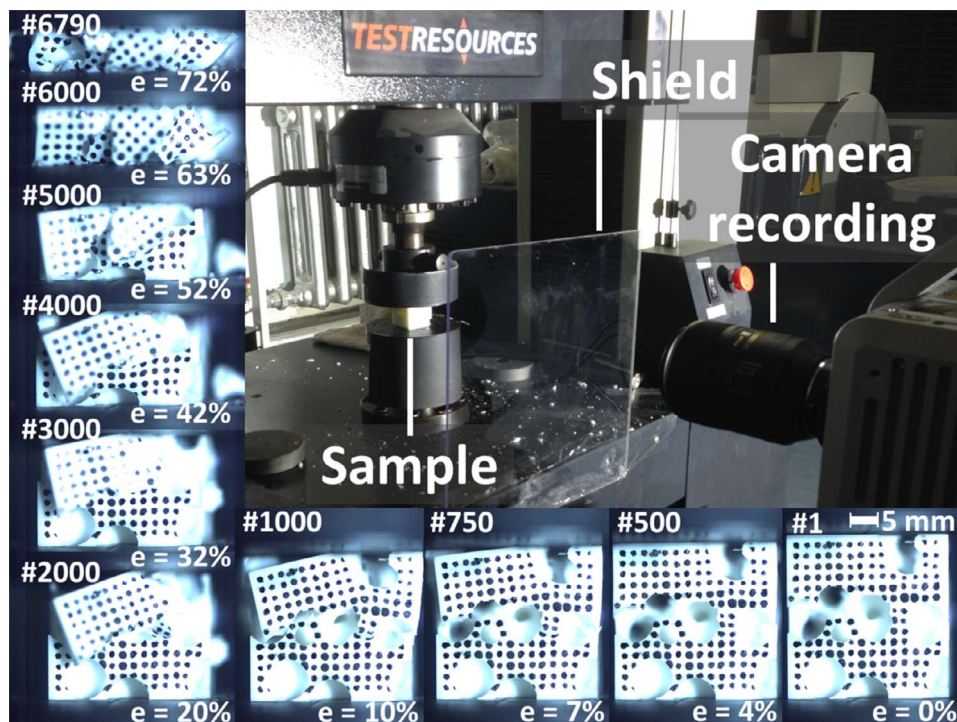


Fig. 3. Compression testing setup of SL-based cellular polymer with illustration of image recording for sample R60A (porosity content 60%). The symbol # encodes the frame number, e is the load level or height reduction percentage. The dots are used for visual guidance (dot spacing close to 2 mm).

slicing resolution of 0.1 mm. The UV radiation is absorbed by the photopolymer to achieve a solid structure. After a solid layer is formed, the supporting platform is moved away from the surface and then the next layer is cured. These steps (the movement of the platform and the curing of an individual pattern in a layer of resin) are repeated layer by layer until the part is completely built. Due to the risk of structural collapsing during the process especially with cellular materials, support is added, which is formed by thin struts of the same resin and cured using the same process of laser beam exposure. Fig. 2 illustrates the principle of SL process including the support structure generation. Finally, the part is exposed for about 16 min. to high intensity ultraviolet radiation in order to complete the curing process and gain more structural stability [21]. More than 60 specimens are fabricated under the same conditions and process parameters.

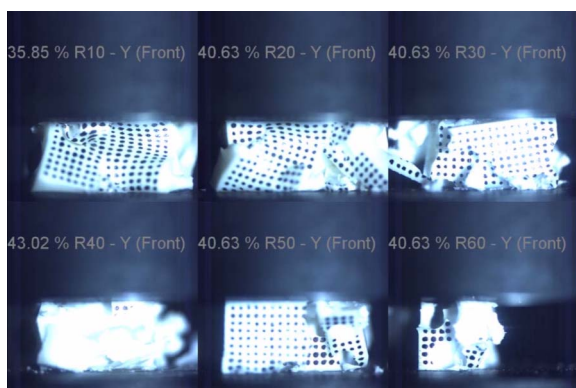
## 2.2. Characterisation protocols

Compression testing of the SL cellular blocks is performed using an electromechanical universal test machine from Testresources Inc. (Shakopee, MN, USA), equipped with a load cell of 100 kN (Fig. 3). Loading is performed up to densification under a load rate of 10 mm/min.

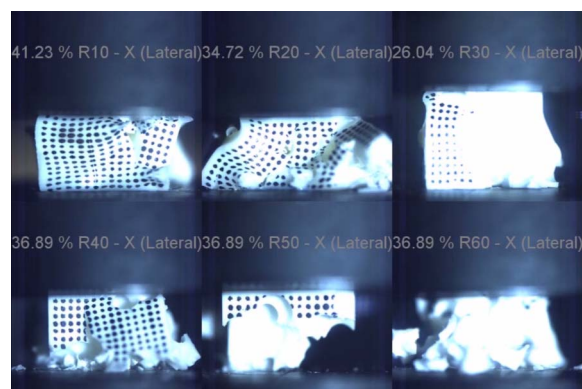
Uniaxial loading is performed on all orthogonal faces including the building direction to reveal any anisotropy in mechanical behaviour. These correspond to uniaxial loading in X-direction (lateral face), Y-direction (front face) and Z-direction or building direction (top face). Optical imaging of the lateral view of the samples is conducted simultaneously using a high-speed camera (Fastcam SA-X2 from Photron company, USA) with a spatial resolution of  $900 \times 900$  pixels and a frame rate of 50 fps. Supplementary materials as video recordings of all loading situations are provided for all studied SL-based cellular materials (refer Videos 1–3).



Movie 1.



Movie 2.



Movie 3.

In addition to mechanical testing, X-ray micro-tomography imaging of SL cellular structures is considered using UltraTom X-ray micro-CT instrument (Fig. 4). Acquisition parameters are: 230 kV X-ray source, 60 kV (voltage), 480  $\mu$ A (current intensity), 31  $\mu$ m (voxel size). 3D images of typical resolution of one billion voxels are built using X-Act software from Rx-Solutions. Images are processed using ImageJ free software from NIH (USA). Part of the processing is the determination of axial porosity profiles, defect and porosity content and feature size distributions.

Fig. 5 illustrates the rendering of X-ray micro-tomography imaging of studied cellular structures.

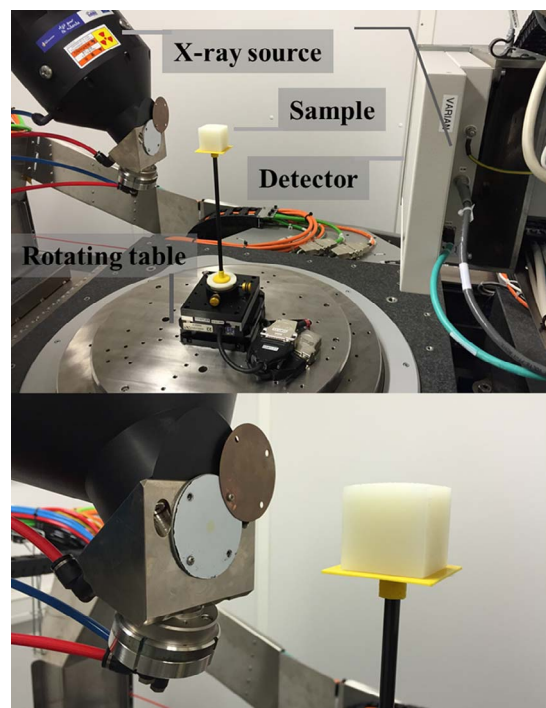


Fig. 4. X-ray micro-tomography imaging illustrated for cellular sample R00.

## 3. Modelling technique

All finite element computations are conducted using Ansys software (PA, USA). Two types of modelling are considered. The first one uses explicitly the microstructural information of CAD and X-ray micro-tomography images to assess elasticity response. The second one relies on implicit implementation of microstructural characteristics. It is meant to model the damage and densification behaviour of the studied cellular structures.

For the first computations, geometry of CAD models and 3D images

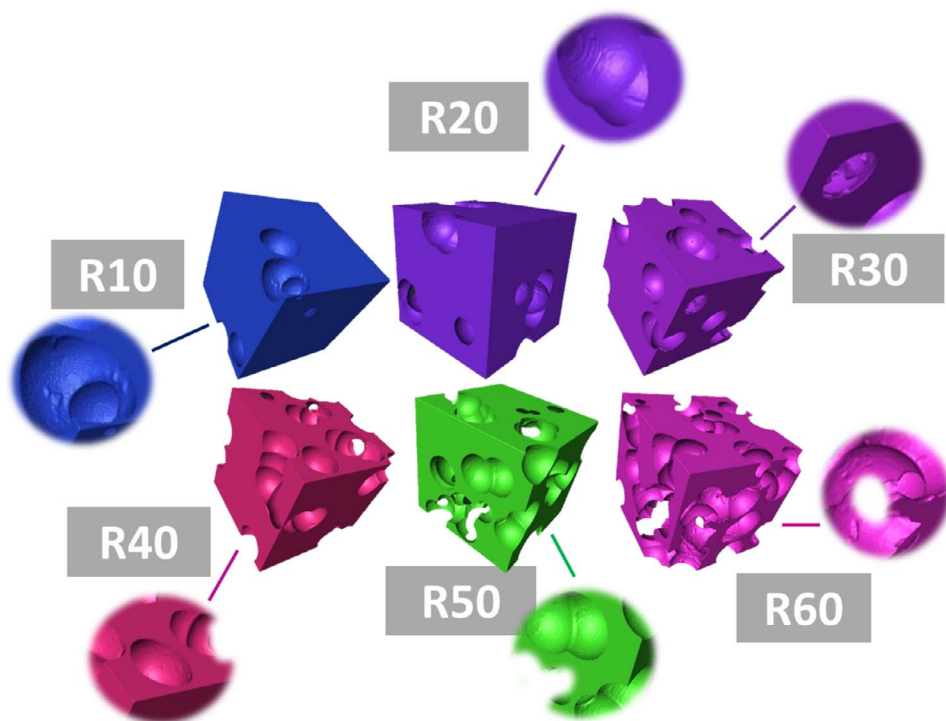


Fig. 5. 3D views of SL-based cellular materials. The numeric value in sample nomenclature refers to the porosity content in percent.

of microstructure of printed SL cellular structures are converted into surface meshing. These meshes are further processed into volume meshes using tetrahedral elements. These elements are defined using four nodes, and each node is described by three degrees of freedom (dof), namely structural displacements  $(u_x, u_y, u_z)$ . Meshing is irregular, which means that its fineness is adapted depending on both local curvature and size of the walls composing the solid phase in the cellular material. The model size varies between  $0.72 \times 10^6$  dof and  $2.41 \times 10^6$  dof. The implemented material model corresponds to the properties of the cured resin. Preliminary analysis of the compressive response of the cured resin shows that it can be considered as an isotropic elastic material defined by a unique couple of Young's modulus ( $E_0 = 1.06 \pm 0.02$  GPa) and Poisson's ratio ( $\nu_0 = 0.23 \pm 0.01$ ). Indeed, Young's moduli values  $1.04 \pm 0.02$  GPa,  $1.07 \pm 0.00$  GPa and  $1.07 \pm 0.00$  measured in X, Y and Z directions confirm a scatter of less than 2%. Also, the six Poisson's ratios derived from measurement of the lateral expansion in the elasticity stage are slightly different  $\nu_{xz} = \nu_{zx} = 0.24 \pm 0.01$ ,  $\nu_{xy} = \nu_{yx} = 0.22 \pm 0.03$ ,  $\nu_{yz} = \nu_{zy} = 0.22 \pm 0.04$ .

To ensure convergence, boundary conditions are adapted to allow sufficient node constraining especially for cellular materials with large amount of voids. Preliminary computations are performed to examine the effect of increasing the layer thickness on which compression boundary conditions are applied. Here, the same axis nomenclature used for experiments applies for simulations. For a loading in Z-direction (building direction), this writes:  $u_z = 0$  for  $0 \leq z \leq Zh$  and  $u_z = -\Delta u$  for  $Z \times (1-h) \leq z \leq Z$  where  $hZ$  is the thickness of the nodal layer in Z-direction subject to uniaxial loading,  $Z = 30$  mm and  $\Delta u > 0$ . Reaction forces are evaluated and Young's moduli in main directions are derived. Fig. 6 shows the predicted Young's moduli in X, Y and Z directions for the case cellular structure containing the largest amount of porosity (R60A).

Young's moduli are more sensitive to boundary conditions when the constrained layer represents less than 1% of the total dimension on which the uniaxial loading is applied. As illustrated in the same sketch, the load transfer materialised by the displacement field becomes effective when a sufficient number of nodes is activated on the loaded surfaces. For the remaining computations,  $h = 5\%$  is selected for each porosity level. This represents 21 different cases to be evaluated (i.e.,

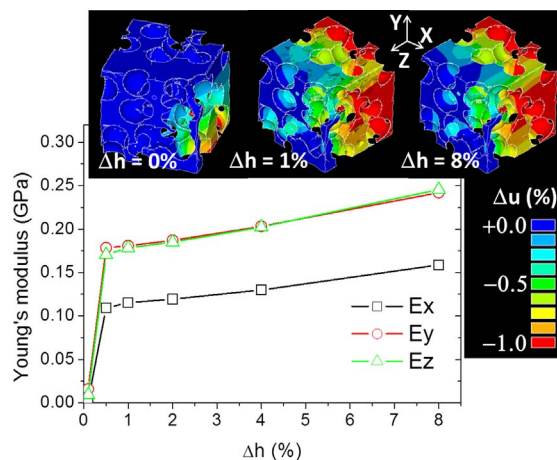


Fig. 6. Preliminary analysis of boundary condition effect on predicted Young's moduli. The largest porosity content is used (R60) with an increasing thickness  $h$  of constrained nodes.

Loading on three orthogonal faces multiplied by the seven studied cellular structures). The computation duration for one uniaxial loading simulation varies between 3 min. and 12 min. depending on model size. Computation performance is measured on a workstation equipped with a pair of 10-core Xeon E5-2620 v3 clocked at 2.3 GHz and 192 GB of RAM.

The second type of computations combines the opposing effects of damage and densification. The increase of stiffness due to cell contact behaviour of the cellular material can be modelled using the expression [22]

$$E_1(\varepsilon(\%)) = E_D \times ((1 - \exp(\varepsilon/100))/(1 - \exp(1)))^d \quad (1)$$

where  $E_1$  is the modulus that accounts for the stiffness increase due to cell wall contact. This modulus depends on the applied load  $\varepsilon$ .  $E_D$  and  $d$  are two coefficients to be identified for each printing configuration.  $E_D$  has the meaning of a densification modulus and can be fairly compared to Young's modulus of the dense phase ( $E_D \approx E_0$ ),  $d$  is the

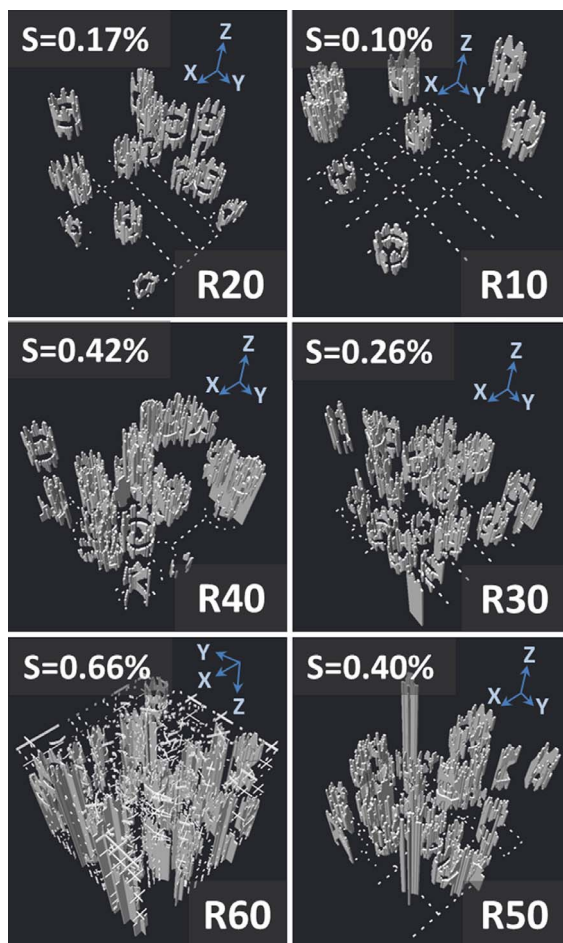


Fig. 7. Support architecture generated during the slicing process as function of porosity content represented by the numeric value XX in the label RXX. S refers to the support volume content.

densification exponent, which triggers the densification onset. In particular, for small loads, the contribution of the densification term is insignificant and starts to be predominant at large loads. The densification coefficient is dependent thus on the characteristics of the printed cellular materials.

Due to the relative brittle nature of the resin, surface creation follows the cell wall rupture events. In order to account for the local lowering of stiffness, another term is added to the overall stiffness of the cellular material

$$E_2(\varepsilon(\%)) = E_R + B_R \times \exp(-A_R \times (\varepsilon - \varepsilon_0)), \varepsilon \geq \varepsilon_0 \quad (2)$$

where  $E_2$  is the damage term, which also depends on the applied load,  $E_R$  is the residual stiffness of the damaged structure,  $\varepsilon_0$  is the strain level at which damage occurs, it can be fairly compared to a yield strain ( $\varepsilon_0 \approx \sigma_Y/E_0$ ) although plasticity effects are neglected,  $A_R$  and  $B_R$  are two coefficients that are identified from the fitting procedure.

## 4. Results and discussion

### 4.1. Microstructural features

Fig. 7 illustrates the support structure generated during the slicing process for all cellular structures. Most of this structure appears as columnar directed towards the building direction.

The remaining part is a grid generated at the base to ease the part collection after curing. The small amount of support (< 0.70%) is justified by the discontinuous nature of all support segments connecting the internal cell walls. The correlation between the amount of support

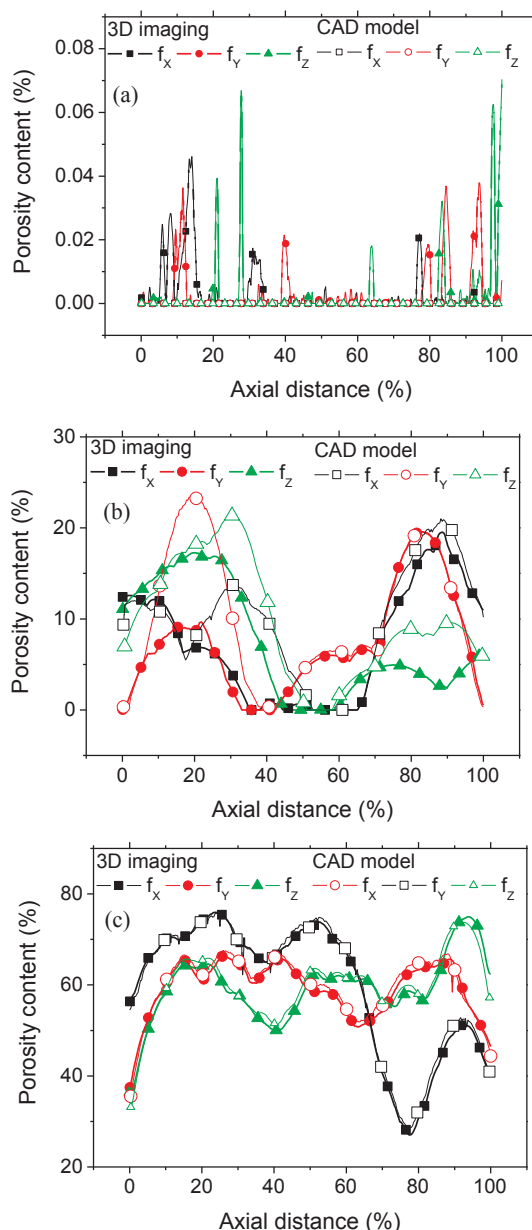


Fig. 8. Axial profiles of porosity content of SL-based cellular structures: comparison between CAD models and real parts imaged using X-ray micro-tomography: (a) R00, (b) R10, (c) R60.

( $S$ ) and the intended porosity content ( $f$ ) can be fairly approximated using a linear profile

$$S(\%) \approx 0.01 \times f(\%); R^2 = 0.94 \quad (3)$$

In order to evaluate whether SL processing induces major violation to the rendering of CAD models of the cellular structures, reference must be made to porosity features. Fig. 8 compares the porosity level profiles measured on both CAD models and 3D images of SL-based cellular structures in X, Y and Z-directions. These profiles are built by measuring, in the three orthogonal directions, the surface content of porosities within each cross-section from both the manufactured SL-cellular structure and the CAD model. Fig. 8 summarises three typical cases among the seven studied conditions: process-induced porosity represented by R00 (Fig. 8a), SL-based structure with dilute porosity population (R10 as Fig. 8b) and percolating porosity network in R60 (Fig. 8c). From Fig. 8a, it is clearly demonstrated that SL-processing does not generate a significant porosity level compared to AM processes

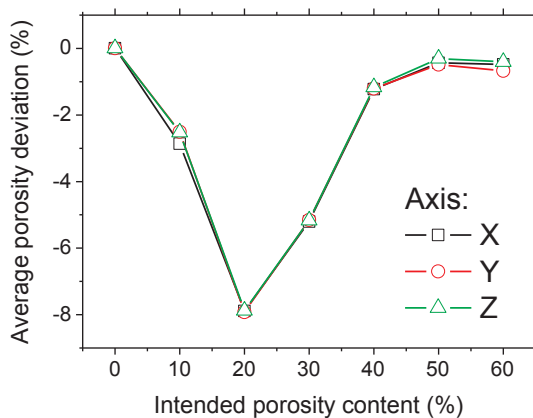


Fig. 9. Average porosity content deviation derived from differences in axial porosity contents in X, Y and Z (building) directions.

such as FDM [23]. This is mainly due to the liquid state which causes limited porosity to appear during the polymerisation process. The minor porosity left behind ( $f < 0.01\%$ ) originates from trapped bubbles in the liquid resin. More contrasted profiles are observed between the CAD model and 3D image for R10 (Fig. 8b). In this dilute porosity situation, most of the bulk porosities have no connection to external surfaces. This means that a large part of the liquid resin is trapped inside these porosities, which explains the relative lower porosity levels measured on the real part (Fig. 8b). Fig. 8c illustrates, however, a perfect matching between the CAD model and the SL-based structure by referring to the same cause that the resin inside the open porosities is

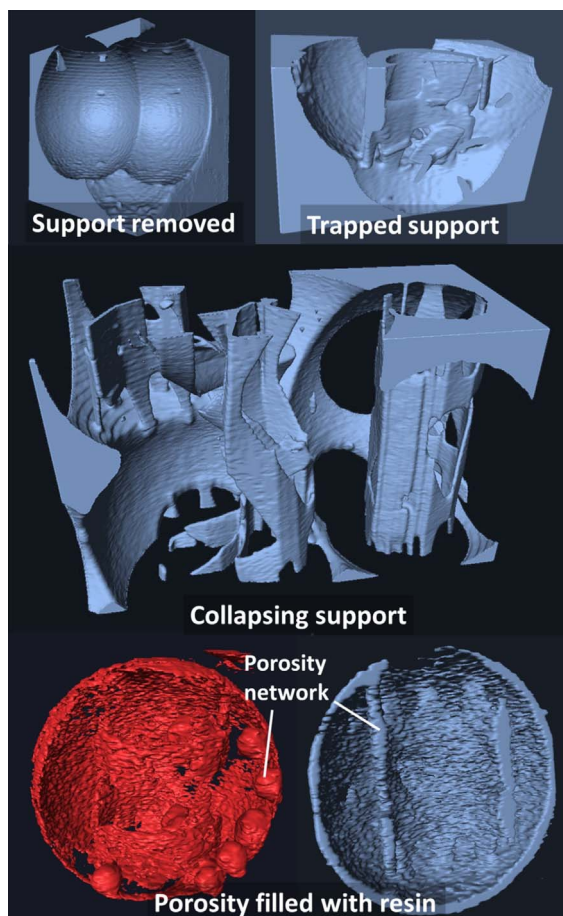


Fig. 10. Typical defect situations induced by stereolithography from X-ray micro-tomography imaging.

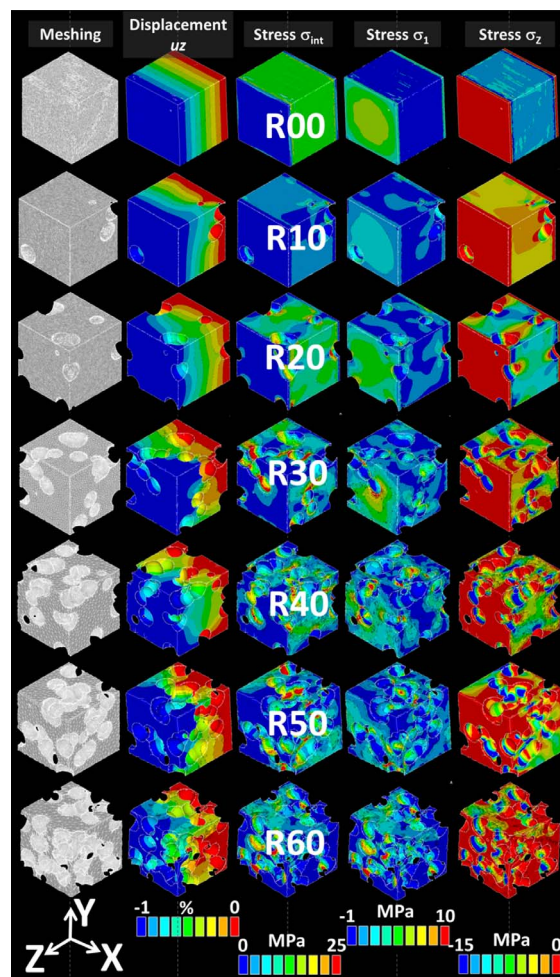


Fig. 11. Nodal solutions for a loading in Z-direction of SL-based cellular structure as function of porosity content (X-ray micro-tomography based FE simulations).

able to be removed.

A more synthesized view including all remaining cellular structures is given in Fig. 9.

The difference between porosity profiles is measured using the area under the curve. Average porosity deviation is derived by dividing the area under the curve by the cellular structure size in X, Y and Z directions. The worst design case corresponds to intended porosity content of 20%. Here the largest amount of resin is trapped inside the porous structure during the processing. Deviations below 2% are observed when the intended porosity content is either below 8% or exceeding 38%. This result remains true for any attempted direction of measurement. Fig. 10 illustrates the main reasons for porosity deviation results.

On the top left side, a successful support removal is reported for open porosities more particularly at the external surfaces. Because the same resin is used for supporting the cellular structure, some residual support hangs over the cell walls. The top right side in Fig. 10 highlights trapped support situation within a closed cell. The central view shows some of the supporting structure collapsed during polymerisation. The former situations can be considered as having a secondary effect on porosity content deviation because of the small amount of support material involved. However, the two bottom views in Fig. 10 hold most of the explanation. These are negative views of what should be the void space inside closed porosities. The solid frame represents here the residual porosity left behind the resin flow inside spherical porosities. This severely damaged cellular structure is reported more particularly for an intended porosity of 20% (Fig. 9).

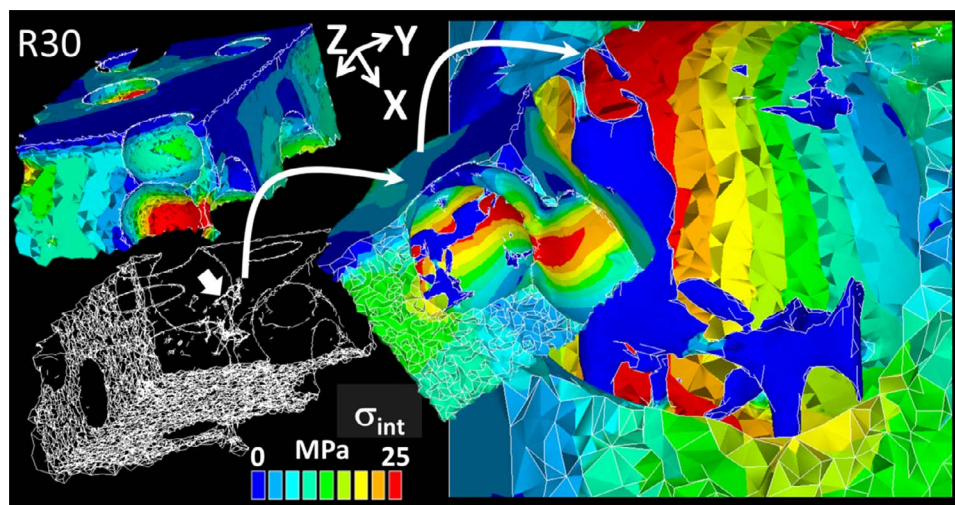


Fig. 12. Magnified view of stress intensity distribution showing the local stress field close to a residual support structure (FE simulation based on X-ray micro-tomography images).

#### 4.2. Mechanical behaviour

Typical nodal solutions of the predicted elasticity behaviour of SL-based cellular structures are shown in Fig. 11. These counterplots are issued for a loading in Z- (building) direction based on the implementation of X-ray micro-tomography images. Displacement component counterplots show uniformly loaded external surfaces for all porosity content conditions. This is related to the thick layer of nodes constrained against loading, which represents 10% of the cellular structure size ( $2 \times h = 10\%$ ). Stress results exhibited using the same magnitude scaling shows a more heterogeneous stress distribution taking place for increasing porosity content. This heterogeneity is

related to the increasing number of stress concentrators. For all studied situations, there is no marked heterogeneity in the building direction (Z), in contrast to recently reported results on FDM [24]. This is explained by the resin continuity ensured during the motion of the moving platform in SL process.

Fig. 12 shows the stress intensity field in the vicinity of a residual support structure for a cellular structure containing 30% of porosities. The low stress levels observed in the support structure demonstrates the minor role of such residual on the compressive response of the cellular structure.

Fig. 13 compares the predicted FE elasticity response of the SL-based cellular structures with the experimental trends.

All sketches are prepared by replacing the porosity content  $f(-)$  by its complementary quantity, namely the relative density  $\rho(-)$ , where  $\rho = 1 - f$ . Here, both X-ray micro-tomography images and CAD models are used as inputs in the FE simulations. Due to the fact that cellular structure is generated randomly with sphere-like overlapping porosities, any expected anisotropy would come from the intrinsic phase properties or induced by the SL process. The nodal solutions shown earlier and the general trend for all simulations and experimental responses show no proof of major anisotropy induced by processing. Also, the relative difference in porosity content between CAD models and real parts, more particularly for  $f = 20\%$ , induces only a shift in Young's moduli trends. Minor differences are found between simulation results and the experimental responses in all tested directions. These differences refer to underestimation of the predicted stiffness response at low relative density values ( $\rho < 0.7$ ) and an overestimation of the same quantity for  $\rho = 0.9$ . The general trend of the simulation results can be easily captured using a linear function in the range  $\rho \in [0.5, 1.0]$ . However, to be more consistent with the cellular material theory, the

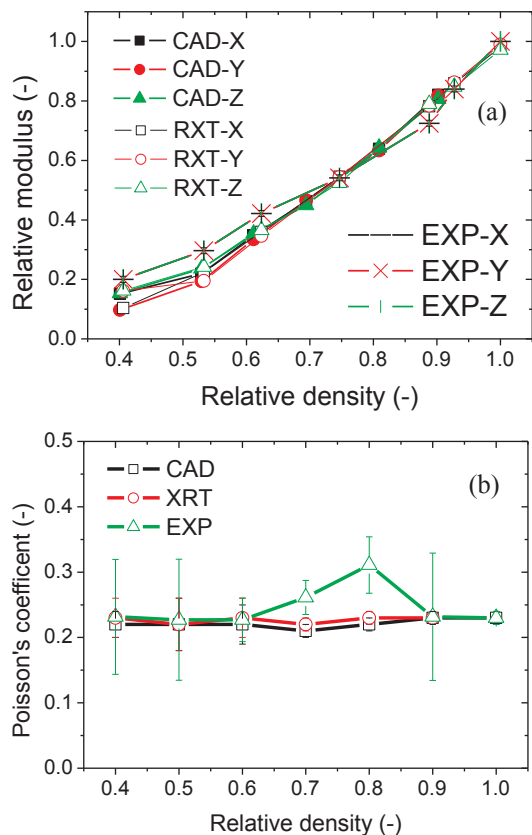


Fig. 13. Elasticity scaling law of SL-based cellular structures: comparison between experimental responses (EXP), CAD models (CAD) and X-ray micro-tomography imaging (RXT) based FE simulations (a) Young's modulus, (b) Poisson's coefficient.

Table 2  
Coefficients ( $\alpha, \beta$ ) of the scaling laws representing the elasticity behaviour of SL-based cellular structures fitted from experimental and FE simulations. The correlation factors  $R^2$  is shown for each evaluation in X, Y and Z (building) directions.

Axis	X			Y			Z (building)		
	$\alpha_X$	$\beta_X$	$R_X^2$	$\alpha_Y$	$\beta_Y$	$R_Y^2$	$\alpha_Z$	$\beta_Z$	$R_Z^2$
Experimental	1.76	0.97	0.99	1.76	0.97	0.99	1.76	0.97	0.99
FE simulation - CAD based	2.15	1.00	0.99	2.68	1.06	0.99	2.10	0.99	0.99
FE simulation - X-ray $\mu$ -tomography based	2.49	1.02	0.99	2.19	0.99	0.97	2.07	0.99	0.99

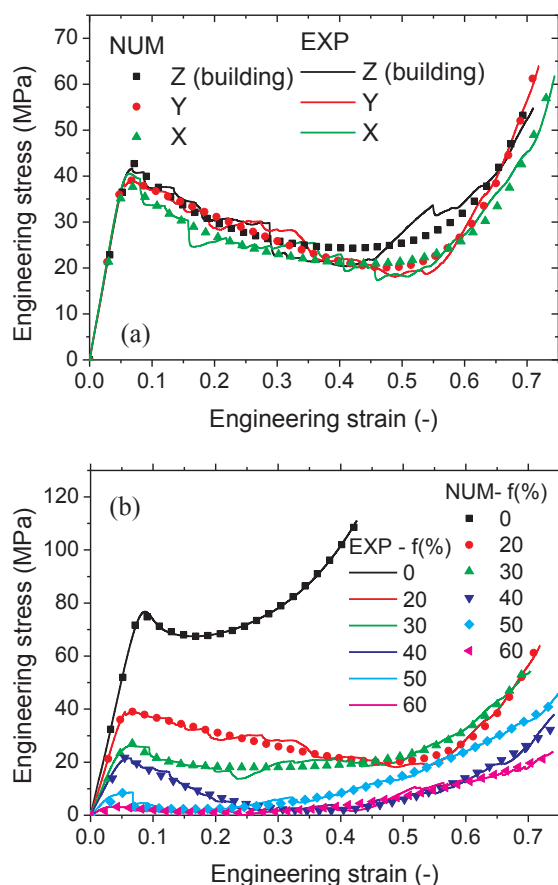


Fig. 14. (a) Isotropy of a SL-based cellular structure containing 20% of porosity confirmed through compression response up to densification in X, Y and Z-directions. NUM and EXP stand for finite element predictions (NUM) and experimental observation (EXP), (b) comparison between experimental and numerical trends of SL-based cellular structures as function of porosity content  $f$ .

following nonlinear function is used

$$E/E_0(-) = \beta \times \rho(-)^\alpha \quad (4)$$

where  $(\alpha, \beta)$  are coefficients directly available from the fitting of the log – log representation of all trends in Fig. 13a. Table 2 summarises the fitting coefficients for all simulations and experimental results.

The fitting results are all satisfying if we compare the achieved correlation factors for all conditions ( $R^2 = 0.99$ ). Table 2 reports the same magnitude for coefficients derived from the experimental responses in X, Y and Z directions. A stiffer behaviour involving more uniaxial deformation is a distinct feature of the experimental evidence ( $\alpha < 2.00$ ). A typical behaviour of a cellular material accounting for more bending contribution is achieved with the FE simulations ( $\alpha \approx 2.28 \pm 0.25$ ).

Poisson's coefficient predictions related to FE computations of both CAD models and X-ray imaging are compared to experimental data derived from image analysis. Fig. 13b shows that the numerical results are invariant with respect to the relative density. The experimental trend suggests a slight change of behaviour for a relative density between 0.7 and 0.8. An explanation of this change may be related to a possible effect of pore filling experienced within the same range of relative density.

The behaviour of studied SL-based cellular structures up to the densification is further explored in Fig. 14.

In order to confirm the isotropy of cellular structures printed using stereolithography, the mechanical responses in X, Y and Z-directions are compared in Fig. 14a. Both experimental and numerical trends are

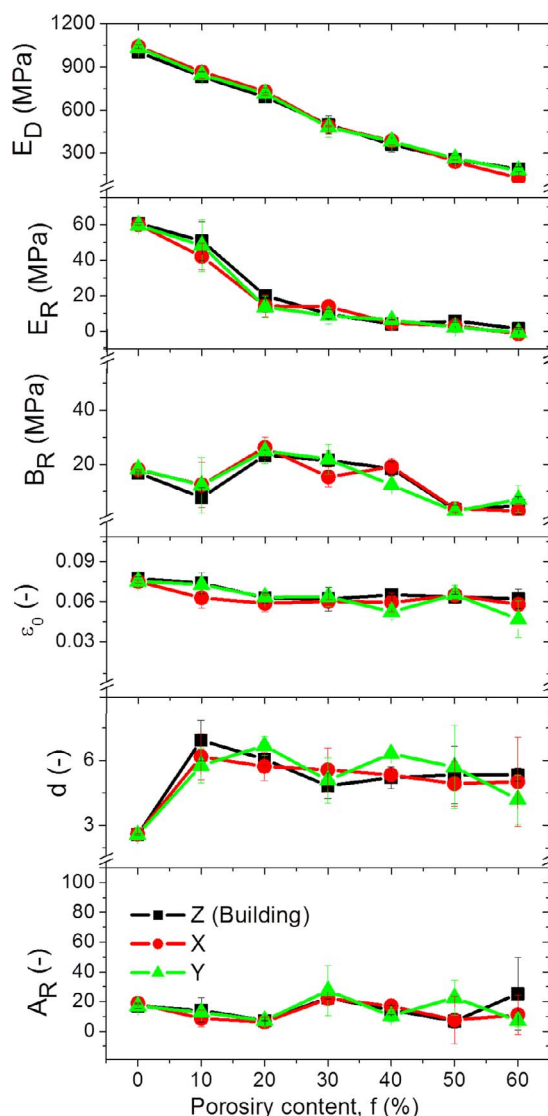


Fig. 15. Scaled quantities used to define the damage-densification law in finite element model as function of porosity content  $f$ .

plotted for a cellular structure containing 20% of porosities. The numerical predictions are based on the damage-densification constitutive law introduced earlier. No major differences between trends in X, Y and Z direction is found confirming the isotropy of SL-based cellular structures. Also, a fair matching between experimental and numerical responses is obtained. All deformation stages up to densification are appropriately captured using the damage-densification constitutive law. The main characteristics of the compressive response are the damage onset in the elasticity stage followed by a descent of the reaction force and finally sharp force increase. To these three stages are associated the following deformation mechanisms: cell wall bending, cell collapse, and cell densification. Minor differences do exist between numerical and experimental trends. These are related to the sudden changes in reaction force evidenced experimentally, which reflect mechanical instabilities driven by cell wall rupture events. From the numerical viewpoint, rupture event are treated as local change in stiffness and correspond to a smoother change in reaction force.

Fig. 14b compares the compression response of SL-based cellular structure as function of porosity content. The typical behaviour introduced earlier is confirmed with some differences related to a decreasing stress magnitude at damage onset, lower stress level in cell collapse regime and lower stress rate increase at densification, all

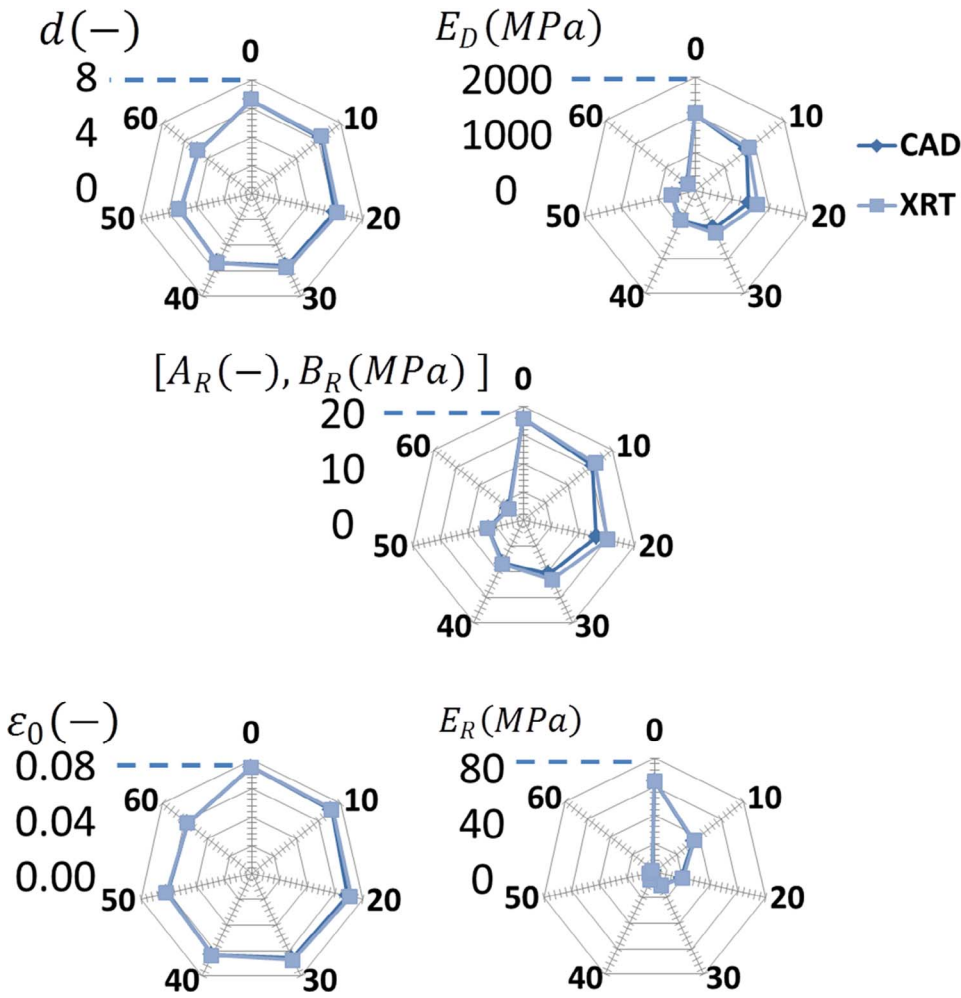


Fig. 16. Radar charts of the six mechanical parameters of the damage – densification law showing the difference between CAD models and real parts (XRT: X-ray micro-tomography imaging).

related to the increase of porosity content. The numerical predictions capture fairly all trends as function of porosity content with minor issues related to the instable change in reaction forces discussed earlier.

The fair agreement between experimental and numerical trends is based on adjustment of the six mechanical parameters associated to the damage-densification constitutive law, namely,  $E_D$ ,  $E_R$ ,  $B_R$ ,  $\varepsilon_0$ ,  $d$ ,  $A_R$ . These parameters are further correlated to the amount of porosity in the SL-based cellular structures as shown in Fig. 15. The identification of all parameters is performed using the mechanical response of 64 replicates for testing in X, Y and Z directions. The identified parameters all show minor dependence on testing direction as attested by the analysis of average and standard deviation. The first parameter,  $E_D$  shown on the top of Fig. 15 represents the densification modulus.

A large porosity content delays the densification because a larger space is available for structural displacement of cell walls before contact. Consequently,  $E_D$  decreases. The negative trend can be fairly approached using a linear function of the form:

$$E_D \text{ (MPa)} = 1011 - 15 \times f(\%); R^2 = 0.99 \quad (5)$$

The second coefficient of the densification term,  $d$  follows a similar trend if we exclude the first point ( $f = 0\%$ ). This parameter is found to decrease with the increase of the porosity content

$$d(-) = 6.57 - 0.03 \times f(\%); R^2 = 0.68 \quad (6)$$

The second parameter,  $E_R$  plotted against the porosity content refers to the residual stiffness of the damaged cellular structure. This residual stiffness is affected by the initial stiffness and damage accumulation during loading. From Fig. 14, minimum reaction forces reach ground

values for porosity levels as large as 40%. This causes the residual stiffness to be nonlinearly correlated to the porosity level. In Fig. 15, this can be captured using a decay function of the form

$$E_R \text{ (MPa)} = 64 \times \exp[-0.06 \times f(\%)]; R^2 = 0.95 \quad (7)$$

Both parameters  $A_R$  and  $B_R$  of the damage term in Eq. (2) are found to exhibit the same behaviour ( $A_R \approx B_R$ ). These two parameters control the rate, width and overall trend of the cell collapse stage. With a jagged variation with respect to the porosity content, a linear decreasing profile is fairly obtained

$$[A_R(-), B_R \text{ (MPa)}] = 18 \times [(-), \text{(MPa)}] - 0.25 \times f(\%); R^2 = 0.73 \quad (8)$$

The damage onset represented by the quantity  $\varepsilon_0$  slightly changes with respect to the porosity content. A linear correlation is predicted for this parameter

$$\varepsilon_0(-) = 0.075 - 3 \times 10^{-4} \times f(\%); R^2 = 0.80 \quad (9)$$

Based on the fact that defects induced by stereolithography are more related to shifts in porosity content (Fig. 9), it is possible to compare the compressive response of CAD models and real parts using X-ray micro-tomography results. With the help of the identified parameters of the damage – densification model and related correlations, the radar charts in Fig. 16 show the variation of the six parameters of the damage – densification model using porosity levels derived from CAD and XRT (X ray micro-tomography).

The average variation of the six parameters as a result of change in porosity content is less than 7%. The cellular material standing apart from the group is the one containing 20% of porosities. The difference

between CAD and XRT represents, respectively, 14%, 13%, 5%, 4%, 3% for  $E_D$ ,  $A_R$  and  $B_R$ ,  $E_{R,d}$ , and  $\epsilon_0$ .

## 5. Conclusions

This study shows that X-ray micro-tomography proves to be a key technique to sense microstructural differences between CAD models and real printed designs. Imaging results demonstrate that the design of cellular polymers containing randomly distributed spherical voids using stereolithography (SL) has to be considered with care especially in terms of intended porosity content. The considered SL setup, with a descending printing base, results in deviation in 8% of porosity content for an intended porosity level of 20%. In the porosity content range 10–30%, the achieved low porosity contents are due to excess of resin flowing into the closed porosities during the building process. SL-based cellular polymers with larger intended porosity contents allow the evacuation of resin excess thanks to the increasing pore connectivity. X-ray imaging combined with finite element computations show also that the amount of residual support material has minor mechanical effect. The same material elasticity law is achieved for CAD-based and 3D imaging-based FE computations with shifts on Young's modulus related to the porosity content deviation. Poisson's expansion of the printed cellular structures seems to be invariant with respect to porosity content. Constitutive modelling of the compressive behaviour up to densification reveals no mechanical anisotropy. The implemented damage – densification model captures all deformation stages up to densification for any porosity level in the range 0–60%.

This study concludes finally that mechanical defects induced by stereolithography can be anticipated by adjusting the porosity level in an appropriate range without much affecting the trend of the compressive behaviour.

## Declaration of interest

The authors declare no conflict of interest.

## Author contributions

Dr. Sofiane Guessasma contributed to the overall management of the processing, microstructural and mechanical testing experiments including protocol and campaign designs. He also performed the analysis and interpretation of X-ray micro-tomography data, finite element computations, experimental results and drafting the article. M. Liu Tao was in charge of the processing of cellular materials, acquisition of mechanical tests and analysis, and partly drafting the manuscript. Dr. Sofiane Belhabib performed the design of airy structures and contributed in drafting the manuscript. Dr. Hedi Nouri contributed to the conception and acquisition of X-ray micro-tomography experiments. Prof. Jihong Zhu contributed to the management of 3D printing and mechanical testing experiments. Prof. Weihong Zhang contributed to the management of the processing and testing of cellular materials.

## Funding source

This work is partly supported by National Key Research and

Development Program (2017YFB 1102800) and National Natural Science Foundation of China under the grant numbers 111722219, 11432011, 1620101002.

## References

- [1] L.J. Gibson, M.F. Ashby, *Cellular solids. Structure and properties*, second ed., Cambridge Press University, 1997.
- [2] H. Altenbach, *Mechanics of advanced materials for lightweight structures*, Proc. Inst. Mech. Eng., Part C: J. Mech. Eng. Sci. 225 (11) (2011) 2481–2496.
- [3] Y.H. Wang, J.P. Lin, Y.H. He, C.K. Zu, G.L. Chen, Pore structures and thermal insulating properties of high Nb containing TiAl porous alloys, *J. Alloys Comp.* 492 (1–2) (2010) 213–218.
- [4] J.P. Arenas, M.J. Crocker, Recent trends in porous sound-absorbing materials, *Sound Vib.* 44 (7) (2010) 12–17.
- [5] S.J. Hollister, Porous scaffold design for tissue engineering, *Nat. Mater.* 4 (7) (2005) 518–524.
- [6] E.O. Olakanmi, R.F. Cochrane, K.W. Dalgarno, A review on selective laser sintering/melting (SLS/SLM) of aluminium alloy powders: processing, microstructure, and properties, *Progr. Mater. Sci.* 74 (2015) 401–477.
- [7] I. Gibson, D.W. Rosen, B. Stucker, *Additive Manufacturing Technologies*, Springer, 2010.
- [8] F.P.W. Melchels, J. Feijen, D.W. Grijpma, A review on stereolithography and its applications in biomedical engineering, *Biomaterials* 31 (24) (2010) 6121–6130.
- [9] S. Corbel, O. Dufaud, T. Roques-Carnes, *Materials for Stereolithography*, in: P.J. Bártolo (Ed.), *Stereolithography: Materials, Processes and Applications*, Springer, 2011, p. 141.
- [10] J.Y.H. Fuh, S. Chew, Curing characteristics of acrylic photopolymer used in stereolithography process, *Rapid Prototyping J.* 5 (1) (1999) 27–34.
- [11] P. Mohan Pandey, N. Venkata Reddy, S.G. Dhande, Slicing procedures in layered manufacturing: a review, *Rapid Prototyping J.* 9 (5) (2003) 274–288.
- [12] J.G. Zhou, D. Herscovici, C.C. Chen, Parametric process optimization to improve the accuracy of rapid prototyped stereolithography parts, *Int. J. Mach. Tools Manuf.* 40 (3) (2000) 363–379.
- [13] K. Chockalingam, N. Jawahar, U. Chandrasekar, Influence of layer thickness on mechanical properties in stereolithography, *Rapid Prototyping J.* 12 (2) (2006) 106–113.
- [14] R. Quintana, J.-W. Choi, K. Puebla, R. Wicker, Effects of build orientation on tensile strength for stereolithography-manufactured ASTM D-638 type I specimens, *Int. J. Adv. Manuf. Technol.* 46 (1–4) (2009) 201–215.
- [15] E.W. Andrews, G. Gioux, P. Onck, L.J. Gibson, Size effects in ductile cellular solids Part II: experimental results, *Int. J. Mech. Sci.* 43 (3) (2001) 701–713.
- [16] J. Parthasarathy, B. Starly, S. Raman, A. Christensen, Mechanical evaluation of porous titanium (Ti6Al4V) structures with electron beam melting (EBM), *J. Mech. Behav. Biomed. Mater.* 3 (3) (2010) 249–259.
- [17] A.P. Roberts, E.J. Garboczi, Elastic properties of model random three-dimensional open-cell solids, *J. Mech. Phys. Solids* 50 (1) (2002) 33–55.
- [18] S. Guessasma, P. Babin, G.D. Valle, R. Dendievel, Relating cellular structure of open solid food foams to their Young's modulus: finite element calculation, *Int. J. Solids Struct.* 45 (10) (2008) 2881–2896.
- [19] G. Campoli, M.S. Borleffs, S. Amin Yavari, R. Wauthle, H. Weinans, A.A. Zadpoor, Mechanical properties of open-cell metallic biomaterials manufactured using additive manufacturing, *Mater. Des.* 49 (2013) 957–965.
- [20] C. Veyhl, I.V. Belova, G.E. Murch, T. Fiedler, Finite element analysis of the mechanical properties of cellular aluminium based on micro-computed tomography, *Mater. Sci. Eng.: A* 528 (13–14) (2011) 4550–4555.
- [21] J.M. Dulieu-Barton, M.C. Fulton, Mechanical properties of a typical stereolithography resin, *Strain* 36 (2) (2000) 81–87.
- [22] S. Guessasma, H. Nouri, Comprehensive study of biopolymer foam compression up to densification using X-ray micro-tomography and finite element computation, *Eur. Polym. J.* 84 (2016) 715–733.
- [23] O.B. Hassana, S. Guessasma, S. Belhabib, H. Nouri, Explaining the difference between real part and virtual design of 3D printed porous polymer at the microstructural level, *Macromol. Mater. Eng.* (2016).
- [24] S. Guessasma, S. Belhabib, H. Nouri, O. Ben Hassana, Anisotropic damage inferred to 3D printed polymers using fused deposition modelling and subject to severe compression, *Eur. Polym. J.* 85 (2016) 324–340.